PCCP

ROYAL SOCIETY OF CHEMISTRY

PAPER

View Article Online
View Journal | View Issue

Cite this: *Phys. Chem. Chem. Phys.*, 2021, **23**, 2676

The H_2^+ + HD reaction at low collision energies: H_3^+/H_2D^+ branching ratio and product-kinetic-energy distributions†

Katharina Höveler, Johannes Deiglmayr,‡ Josef A. Agner, Hansjürg Schmutz and Frédéric Merkt *

The fully state-selected reactions between H_2^+ molecules in the $X^+\ ^2\Sigma_g^+(v^+ = 0, N^+ = 0)$ state and HD molecules in the $X\ ^1\Sigma_g^+(v = 0, J = 0)$ state forming H_3^+ + D and H_2D^+ + H have been studied at collision energies E_{coll} between 0 and k_B·30 K with a resolution of about 75 mK at the lowest energies. H_2 molecules in a supersonic beam were prepared in Rydberg-Stark states with principal quantum number n = 27 and merged with a supersonic beam of ground-state HD molecules using a curved surface-electrode Rydberg-Stark decelerator and deflector. The reaction between H_2^+ and HD was studied within the orbit of the Rydberg electron to avoid heating of the ions by stray electric fields. The reaction was observed for well-defined and adjustable time intervals, called reaction-observation windows, between two electric-field pulses. The first pulse swept all ions away from the reaction volume and its falling edge defined the beginning of the reaction-observation window. The second pulse extracted the product ions toward a charged-particle detector located at the end of a time-of-flight tube and its rising edge defined the end of the reaction-observation window. Monitoring and analysing the time-of-flight distributions of the H_3^+ and H_2D^+ products in dependence of the duration of the reaction-observation window enabled us to obtain information on the kinetic-energy distribution of the product ions and determine branching ratios of the H_3^+ + D and H_2D^+ + H reaction channels. The mean product-kinetic-energy release is 0.46(5) eV, representing 27(3)% of the available energy, and the H_3^+ + D product branching ratio is 0.225(20). The relative reaction rates correspond closely to Langevin capture rates down to the lowest energies probed experimentally (≈k_B·50 mK).

Received 24th November 2020,
Accepted 7th January 2021

DOI: 10.1039/d0cp06107g

rsc.li/pccp

I Introduction

In recent years, studies of collisions and chemical reactions using merged-beams techniques have enabled the investigation of reactions between neutral molecules at collision energies E_{coll} much below k_B·10 K (k_B is Boltzmann's constant) and in some cases even below k_B·1 K.[1–7] In merged-beams studies, the energy resolution can be much enhanced if pulsed valves releasing very short gas pulses are used to generate supersonic beams and the gas pulses are allowed to expand over a long distance between the valve orifice and the reaction region: By exploiting the longitudinal velocity dispersion of the beams, one can make sure that only molecules within a very narrow velocity distribution participate in the reactions.[1,4] Merged-beams studies are thus well suited to study resonance phenomena in the collision cross sections at low collision energies and to study chemical reactions under conditions where quantum effects affect the cross sections.

The study of ion–molecule reactions at low collision energies and low temperature is more challenging than the study of reactions between neutral molecules. Studies at very low collision energies or temperatures are becoming possible in experiments in which (ultra)cold atoms and atomic or molecular ions are trapped in the same volume (see, *e.g.*, ref. 8), but are so far restricted to atoms that can be laser cooled. Temperatures down to about 10 K have been reached in supersonic beams expanding out of Laval nozzles[9] and in ion guides and traps using cold He gas to cool the reactants.[10–12] Until recently, lower temperatures could generally not be reached because stray electric fields in the reaction volume accelerate and heat up the ions. The most important ion–molecule reactions at low temperatures are barrierless, exothermic reactions, for which the rates are expected to be well described by capture models.[13–17] These models predict fast reactions with low-temperature behaviours dictated by the

Laboratory of Physical Chemistry, ETH Zurich, CH-8093 Zurich, Switzerland. E-mail: merkt@phys.chem.ethz.ch

† Dedicated to the memory of Professor Dieter Gerlich.

‡ Present address: Department of Physics, University of Leipzig, DE-04109 Leipzig, Germany.

electrostatic properties of the neutral molecules, *i.e.*, their polarisabilities, dipoles, quadrupoles, *etc.* In fast capture reactions, shape resonances of the kind encountered in reactions between neutral molecules are not expected. However, below 10 K, ion–molecule reactions have been predicted to exhibit strong effects caused by the alignment of the rotational angular momentum vector of apolar neutral molecules and the orientation of polar neutral molecules in the Coulomb field of the ion, see, *e.g.*, ref. 13–25. These effects tend to be strongly dependent on the rotational state of the neutral molecule but have not been systematically studied experimentally yet below 10 K.

A prototypical example of such reactions is the reaction $H_2^+ + H_2 \rightarrow H_3^+ + H$, which plays a key role as initial step of reaction cycles in interstellar clouds (see ref. 26 and references therein). This reaction closely follows Langevin-capture behaviour for reactions with a dominant ion-induced-dipole long-range interaction,[24–28] and only significantly deviates from this behaviour at elevated temperatures[29] or at temperatures much below 1 K.[25,30] The reaction is strongly exothermic, with a 0 K reaction internal energy $\Delta_r U^\circ(0\ \mathrm{K})$ of −1.70 eV, corresponding to the difference between the 0 K dissociation energy of H_2^+[31] and the 0 K dissociation energy of H_3^+ into H_2 and H^+.[32] Product-recoil measurements at collision energies E_{coll} between 1.5 and 5.3 eV in crossed-beams experiments indicate that about a third of the available energy ($E_{coll} + \Delta_r U^\circ(0\ \mathrm{K})$) is released as kinetic energy, two thirds being stored as internal (rovibrational) energy of H_3^+.[33,34] With this reaction, we have recently demonstrated that the ion-heating effects of stray electric fields can be strongly reduced if the ion is replaced by the parent neutral species excited to a high Rydberg state.[30,35] The Rydberg electron, orbiting at large distances from the ion core, does not significantly affect the reactions of the ion core with neutral molecules located within the Rydberg-electron orbit,[36–39] but effectively shields the ion–molecule reaction system from heating effects by stray electric fields. Additionally, Rydberg atoms and molecules have large electric dipole moments, so that inhomogeneous electric-field distributions can be used to manipulate their velocity distribution, in particular to slow down and deflect supersonic beams in free space[40,41] or above the surface of integrated circuit boards.[42] In our studies of ion–molecule reactions, we exploit curved circuit boards as Rydberg-atom[43] and Rydberg-molecule[44] decelerators and deflectors. These devices are ideally suited (i) to merge supersonic beams of Rydberg atoms and molecules with supersonic beams of neutral molecules and (ii) to adjust their relative velocity, and thus the collision energy for studies of ion–molecule reactions at collision energies below $k_B \cdot 1$ K.[30,35,45,46]

In our studies of the $H_2^+ + H_2 \rightarrow H_3^+ + H$ reaction mentioned above, we observed that it is only at collision energies significantly below $k_B \cdot 1$ K that the reaction cross section starts departing from Langevin-capture behaviour.[35] By comparison with theoretical calculations,[24,25] this deviation could be attributed to the alignment, by the joint effects of the ion–quadrupole interaction and Coriolis coupling, of the rotational angular-momentum vector of ortho-H_2 molecules in their $J = 1$ ground state, which formed 75% of the H_2 population in the beam. This effect should not be present in collisions from supersonic expansions of para-H_2 or HD because only the $J = 0$ rotational ground state is populated in such expansions and this state does not have a quadrupole. We present here the results of an experimental investigation of the reaction between H_2^+ and HD at very low collision energies, which we undertook to verify this expectation. In contrast to the $H_2^+ + H_2$ reaction, which has only one product channel ($H_3^+ + H$) at low collision energies, the $H_2^+ + HD$ reaction system has two competing product channels:

$$H_2^+ + HD \rightarrow H_3^+ + D \quad (1)$$

and

$$H_2^+ + HD \rightarrow H_2D^+ + H, \quad (2)$$

next to the charge-transfer reaction channel

$$H_2^+ + HD \rightarrow H_2 + HD^+, \quad (3)$$

which is endothermic by about 10 meV and not observable at the low collision energies (<4 meV) investigated here. The reaction system thus offers the opportunity to determine the branching ratio between the reaction channels (1) and (2) at very low collision energies and under conditions where both reactants are in a single quantum state, their ground rotational state ($N^+ = 0$ for H_2^+ and $J = 0$ for HD). Because H_3^+ acts as very efficient proton donor and is at the origin of important reaction cycles in interstellar clouds, the branching ratios of reactions (1) and (2) at low collision energies are relevant in the context of the deuterium fractionation of hydride molecules in the interstellar space.

Deuteration of the H_2 and H_2^+ reactants has been successfully used to clarify the reaction mechanism in earlier work at higher collision energies.[34,47–50] We have also extended our experimental approach so as to be able to obtain information on the kinetic energy distribution of the product ions, which, through energy-conservation arguments, can be related to the distribution of internal quantum states of the products, as previously demonstrated for these reactions by Pollard *et al.*[34]

II Experiment

The experiments were carried out using a redesigned version of the merged-beams experimental setup used in our previous measurements of the $H_2^+ + H_2 \rightarrow H_3^+ + H$ reaction at low collision energies.[30,35] We refer to ref. 35 for the general description of the experimental apparatus and measurement procedures. Here, we recapitulate the main features of the experimental approach to study ion–molecule reactions at low collision energies and focus on the improvements of the apparatus made for, and on aspects specific to, the present investigation. These improvements have significantly enhanced the stability and performance of the experimental setup and enabled us to improve the collision-energy resolution of the experiment by a factor of about 4, reaching a value of $k_B \cdot 75$ mK at the lowest collision energies. They have also led to a better control and a more precise characterisation of the velocity and

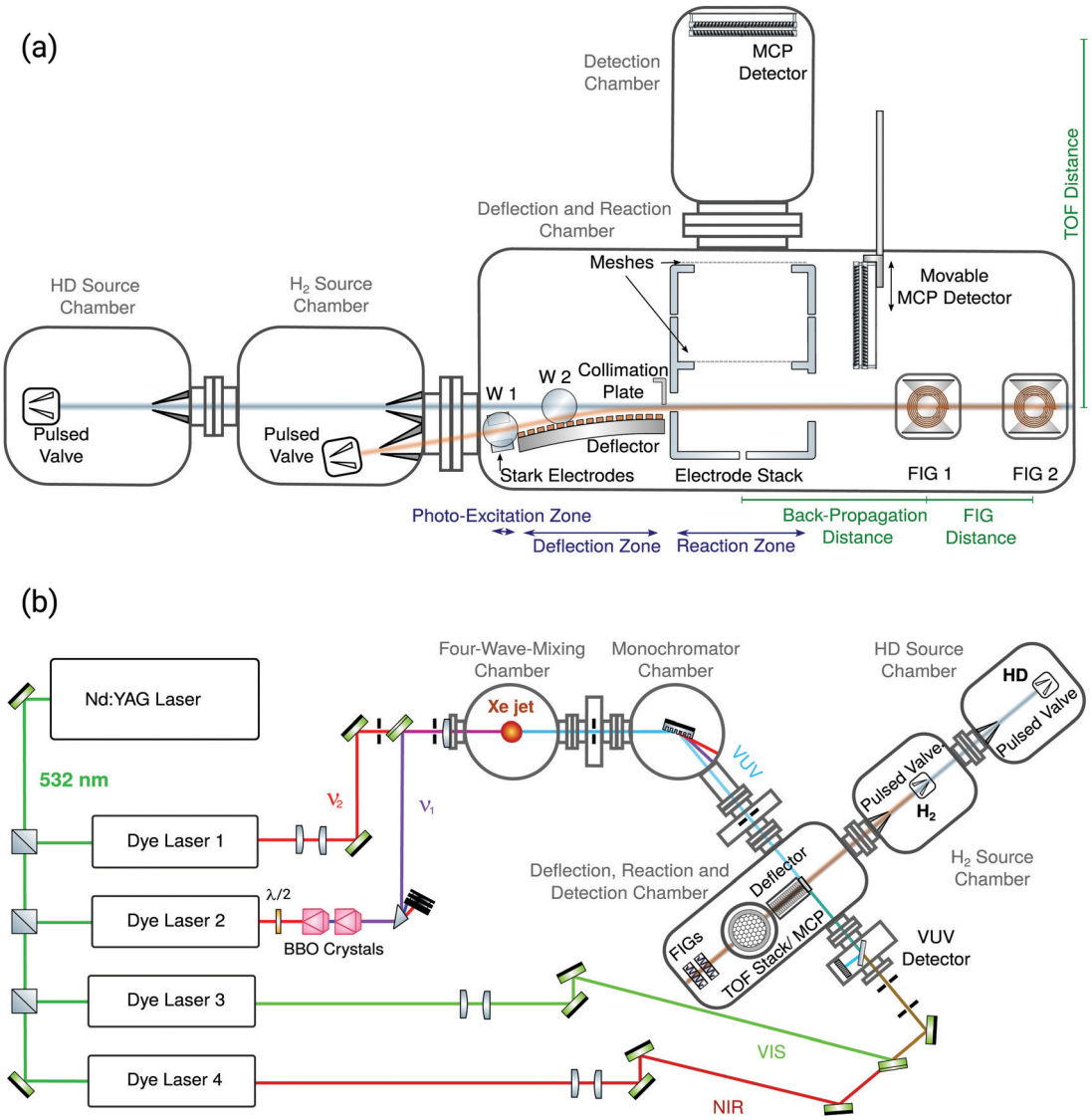

Fig. 1 (a) Side view of the vacuum chambers in which supersonic beams of H_2 and HD are generated with pulsed valves (source chambers), the beams are merged using a Rydberg-Stark deflector and the reaction takes place (deflection and reaction chamber), and the product ions are detected (detection chamber). (b) Schematic aerial view of the merged-beams experimental setup employed to study the H_2^+ + HD reaction at low collision energies, with the laser system used to excite H_2 to long-lived *nk* Rydberg-Stark states through the triply resonant excitation sequence $nkm[X^+(v^+ = 0, N^+ = 0)] \overset{\text{NIR}}{\longleftarrow} I(v = 0, N = 2) \overset{\text{VIS}}{\longleftarrow} B(v = 3, N = 1) \overset{\text{VUV}}{\longleftarrow} X(v = 0, N = 0)$ and the differentially pumped vacuum chambers. FIG: fast ionization gauge; MCP: microchannel plate; TOF: time-of flight; W: window; BBO: beta barium borate; NIR: near infrared; VIS: visible; VUV: vacuum ultraviolet; YAG: yttrium aluminium garnet. See text for details.

spatial distributions of the clouds of reacting molecules. Schematic side and aerial views of the experimental setup are presented in Fig. 1a and b, respectively.

Supersonic beams of HD and H_2 (referred to as the HD and H_2 beams below) are generated in separate source chambers by home-built cryogenic pulsed valves producing short (about 20 μs long) gas pulses and initially propagate along axes separated by 10 degree. Before entering the reaction zone, the HD beam expands into vacuum from a stagnation pressure of 6 bar and passes through two skimmers with orifice diameters of 20 and 3 mm, located 16 and 55 cm downstream of the valve orifice, respectively. A careful optimisation of the properties of the valve-plunger-driving system has enabled the complete suppression of the emission of secondary gas pulses generated by the rebounce of the plunger, which had complicated the analysis of the velocity distributions and reduced the collision-energy resolution of our previous experiments.[30,35] The mean velocity of the gas pulses is set by stabilising the temperature of the valve at any chosen value between 77 and 300 K. For most experiments presented here, the valve was maintained at a temperature of 109 K, corresponding to a mean velocity of 1390 m s^{-1}. We verified that only the $J = 0$ ground rotational state of HD is populated in the HD beam by recording the laser-induced-fluorescence spectrum of the B $^1\Sigma_u^+(v = 4, J') - X\ ^1\Sigma_g^+(v = 0, J'')$

band. The band consisted of a single line, corresponding to the transition from the $J'' = 0$ level of the X state to the $J' = 1$ level of the B state. No transitions could be observed at the position expected for transitions from the $J'' = 1$ ground-state level, from which we conclude that more than 95% of the population of HD molecules in the beam are in the absolute ground state.

The H_2 beam expands from a stagnation pressure of 8 bar and passes through a single skimmer of 2 mm diameter located 16 cm downstream of the valve orifice. The H_2 molecules in this beam are excited to low-field-seeking Rydberg-Stark states with the H_2^+ ion core in its ground X $^2\Sigma_g^+(v^+ = 0, N^+ = 0)$ state and principal quantum number $n = 27$. The photoexcitation is carried out using a triply resonant three-photon excitation sequence using pulsed lasers (repetition rate of 25 Hz, pulse lengths in the range from 2 to 8 ns), as detailed in ref. 51. The photoexcitation takes place between two parallel metallic plates (Stark electrodes in Fig. 1a) used to apply a homogeneous electric field of about 5 V cm^{-1} necessary to make the Rydberg-Stark states optically accessible from the selected $I(v = 0, N = 2)$ intermediate state. At each experimental cycle, about 1000 Rydberg molecules are produced in a volume of about 1 mm^3, as inferred from the strength of the pulsed-field-ionisation (PFI) signal and the numerical particle-trajectory simulations of the Rydberg-Stark deflection process described in ref. 35 and 44 (see also below).

The Rydberg molecules are then loaded into an electric trap moving above a curved surface-electrode Rydberg-Stark decelerator and deflector.[44] The propagation velocity of the moving trap is controlled by applying suitable time-dependent electric potentials to the surface electrodes of the decelerator. This device is used to merge the H_2-Rydberg beam with the HD beam and to adjust the relative mean velocities of the two beams. The H_2 molecules that are not excited by the laser beam propagate in a straight line and are blocked by a collimation slit at the entrance of the reaction zone. This zone is delimited by a cylindrical tube made of three distinct sections to which square-shaped electric-potential pulses are applied to define the interval during which the reaction is monitored (see Fig. 2a). These pulses extract the product ions in a direction perpendicular to the merged-beams propagation axis towards a microchannel-plate (MCP) detector located at the end of a time-of-flight (TOF) tube. In the measurements presented in this article, we monitor the current of product ions impinging on the MPC as we systematically vary selected experimental parameters, such as the relative velocities of the beams, as explained below.

The precise knowledge of the velocity and spatial distributions of the H_2-Rydberg and HD molecules in the beams is crucial because these distributions determine the collision energy and the energy resolution. To determine these distributions we combine measurements, particle-trajectory simulations and extrapolations of distributions measured at different locations, as is now explained in detail. The propagation of the H_2-Rydberg molecules from the entrance of the Rydberg-Stark deflector to the reaction zone is simulated in numerical particle-trajectory calculations,[35,44] which enable us to determine the spatial and velocity distributions of the H_2-Rydberg-molecule cloud in the reaction region.

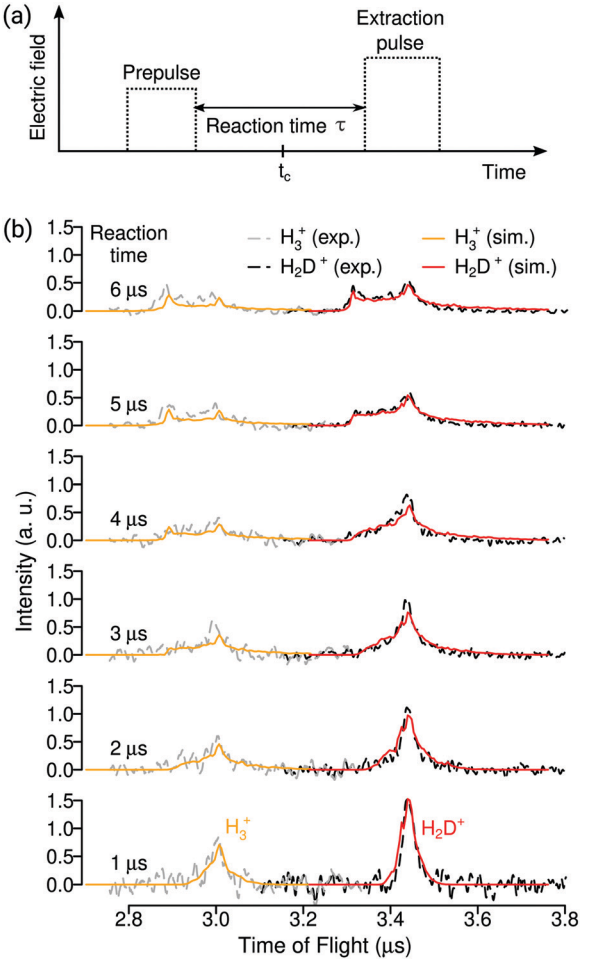

Fig. 2 (a) Two-pulse ion-extraction sequence enabling the control of the duration τ of the reaction-observation window, which we refer to as reaction time. t_c is the time at which the packets of H_2-Rydberg molecules with velocity v_{Ryd} and HD ground-state molecules with velocity v_{HD} reach the centre of the reaction chamber. (b) TOF profiles of the product ions H_3^+ and H_2D^+ generated from the H_2^+ + HD reaction at a collision energy of k_B·1 K for reaction times ranging from 1 to 6 μs. The experimental TOF profiles (grey and black dash-dotted lines for H_3^+ and H_2D^+, respectively) are normalised to the same total integrated product signal and compared to simulated TOF profiles (full orange and red lines for H_3^+ and H_2D^+, respectively). See text for details.

To characterise the H_2-Rydberg-molecule beam, a movable MCP detector is slid into the beam 10.5 cm beyond the centre of the reaction zone and monitors the H_2^+ ions generated by the field ionisation of the H_2-Rydberg molecules close to the MCP surface. Information on the H_2-molecule beam is also obtained from experiments in which the H_2-Rydberg molecules are pulsed field ionised in the reaction zone by applying large electric-potential differences across the extraction electrode stack. The H_2^+ ions produced by PFI are accelerated towards the same MCP detector as used to monitor the reaction products. Following the procedure introduced for studies of the He^+ + CH_3F reaction,[46] we measure the PFI signal as a function of the time delay between the laser pulse and the PFI pulse. In particular, we determine the rise and fall of the PFI

signal as the H_2-Rydberg molecules enter and leave the electrode stack. In this way, we can precisely determine the time t_c at which the H_2-Rydberg cloud is located at the centre of the reaction zone, which we choose as the central time of the reaction-observation temporal window (see Fig. 2a). At the centre of the reaction zone, the Rydberg-molecule cloud forms a 4 mm-long tubular cloud with axis parallel to the laser propagation axis and cross-sectional diameter ($1/e^2$) of about 2 mm. The relative velocity distribution of the H_2-Rydberg molecules in this cloud is determined by the depth of the moving trap, which is itself given by the amplitude of the potential waveforms applied to the decelerator electrodes (see ref. 44). For the experiments presented in this article, the relative-velocity distribution of the H_2-Rydberg molecules exiting the deflector is well described by a thermal distribution corresponding to a temperature of about 75 mK.

In the case of the HD beam, the TOF distributions are monitored by two home-built fast-ionisation gauges (FIGs) located 19.2 and 38.5 cm beyond the centre of the reaction zone. From these distributions and the known positions of both gauges, the relative density and velocity distributions of the HD molecules along the beam-propagation axis can be reconstructed with high accuracy at any point within the reaction zone by backward propagation of their trajectories. The diameter of the HD-molecule cloud in the dimensions perpendicular to the merged-beams propagation direction roughly matches the dimensions of the Rydberg-molecule cloud, but is much longer (several cm) in the dimension parallel to the merged-beams propagation direction as a result of the longitudinal velocity dispersion during the beam propagation. From the knowledge of the spatial and velocity distributions of the HD beam, we can then set the HD-valve trigger so that HD molecules within a well-defined velocity class reach the centre of the reaction zone at the central time of the reaction-observation window. Because of the high degree of transverse collimation by the two skimmers and the large longitudinal velocity dispersion, the velocity distribution of the HD molecules that overlap with the H_2-Rydberg-molecule cloud is much narrower than the velocity distribution of the H_2-Rydberg molecules and corresponds to a temperature of (much) less than 50 mK. The velocity of the reacting HD molecules can be adjusted by changing the HD-valve trigger time relative to the trigger time of the lasers used to photoexcite the H_2 molecules.

The characterisation of both reactant beams allows us to assess the energy resolution of our measurements and its collision-energy dependence, which we find to be given by the equation[46]

$$\frac{\Delta E_{\mathrm{coll}}}{k_{\mathrm{B}}} = \Delta T_{\mathrm{res}} + 2\sqrt{\Delta T_{\mathrm{res}}}\sqrt{\frac{E_{\mathrm{coll}}}{k_{\mathrm{B}}}}, \qquad (4)$$

as long as the duration of the reaction-observation window does not exceed 10 μs. For longer durations, the velocity dispersion of the HD beam needs to be taken into account because it leads to collisions of H_2^+ with HD molecules belonging to different velocity classes, which reduces the collision-energy resolution. In eqn (4), ΔT_{res} describes the distribution of relative velocities of the reaction partners in the merged beam for $E_{\mathrm{coll}} = 0$, which is well approximated by a thermal distribution. In our experiments, ΔT_{res} is about 75 mK and is primarily given by the depth of the moving traps of the Rydberg-Stark deflector. The velocity distribution of the reacting HD molecules hardly makes any contribution because of the large degree of lateral collimation and longitudinal dispersion of the beam, as explained above. The collision-energy resolution of our experiments thus increases from $k_B{\cdot}75$ mK to $k_B{\cdot}2.7$ K as the collision energy increases from 0 to $k_B{\cdot}30$ K.

The duration of the reaction-observation window corresponds to the field-free interval between two square potential pulses we apply to the electrode stack in the reaction zone (see Fig. 2a). The first pulse removes from the reaction zone all ions produced until its falling edge so that this edge defines the beginning of the reaction-observation window. The second pulse then extracts the ions produced during the field-free time between the pulses. The magnitude of the first pulse is chosen to be small enough not to field ionise the H_2-Rydberg molecules. The magnitude of the second pulse should ideally be large enough to field ionise the H_2 molecules and determine their relative density, and also to field ionise the H_3 and H_2D Rydberg-product molecules. In the experiments, we observe that H_3 and H_2D Rydberg-product molecules autoionise very rapidly (within less than 1 μs, as previously observed by Pratt and coworkers[36]) so that the H_3^+ and H_2D^+ product ions can also be extracted with a second pulse of weak electric-field strength. These ions are emitted with considerable kinetic energies so that some product ions can leave the extraction region before the second pulse is applied, particularly for long reaction-observation windows. For short reaction-observation windows, both the Rydberg and the ground-state H_2 densities remain constant to a good approximation, so that the reaction speed is constant. Consequently, when we gradually increase the duration of the reaction-observation window, the product-ion signals first grow linearly until the fastest product ions generated at the beginning of the observation window have left the reaction region by the time the second pulse is applied. The product-ion signals then grow more slowly, reach a maximum and eventually decrease when the reaction-observation window is so long that the entire cloud of H_2-Rydberg molecules has left the reaction zone before the second pulse is applied. The times of flight of the product ions depend on their positions at the time of extraction. Ions that have moved towards (away from) the MCP detector are extracted by smaller (larger) potentials and thus have longer (shorter) flight times. Typical distributions can be seen in Fig. 2b and are discussed in Section III. In our investigations, we use both the time-of-flight distributions of the product ions recorded for different durations of the reaction-observation windows and the deviation from linear signal growth observed for long reaction-observation windows to model the kinetic-energy distributions of the product ions. By energy-conservation arguments, we then derive information on the internal-state distribution of the products.

To determine the collision-energy dependence of the reaction rate coefficients $k(E_{\mathrm{coll}})$, we record the yields of H_3^+ and

H_2D^+ as a function of the difference between the central velocities of the H_2-Rydberg beam and the HD beam. To this end, we keep the central velocity of the HD molecules interacting with the H_2-Rydberg molecules at the centre of the reaction zone constant at the value of 1390 m s^{-1} and vary the velocity of the H_2-Rydberg beam in the range between 1270 and 2020 m s^{-1} by applying suitable potential waveforms to the electrodes of the Rydberg-Stark decelerator and deflector. In this way, we vary the relative velocity $v_{H2} - v_{HD}$ between −120 and 630 m s^{-1} and the collision energy between 0 and k_B·30 K. This procedure requires the adjustment of the trigger time of the HD pulsed valve to make sure that the H_2-Rydberg and HD molecules with the desired velocities reach the centre of the reaction zone at the same time. To obtain reliable values for the rate coefficients, we normalise the product yields through division by the H_2^+ signal generated by PFI of the H_2-Rydberg molecules and the HD signal detected by the fast ionisation gauges. We also subtract the background signal obtained by turning the HD valve off at every second experiment cycle or by shifting its trigger time so that the gas pulses no longer overlap in the reaction zone. This background signal consists primarily of H_3^+ ions from reactions between deflected H_2-Rydberg molecules and H_2 molecules in the background gas.

To determine the branching ratios for reactions (1) and (2), we integrate the normalised ion-TOF signals corresponding to the H_3^+ and H_2D^+ products recorded for different durations of the reaction-observation windows and correct for the loss of products taking place for long reaction-observation windows, as explained in more detail in Section III.

III Results

A. Product-ion time-of-flight distributions and internal energies

Reliable relative reaction cross sections and branching ratios for the two product channels (1) and (2) can only be obtained if the TOF distributions of the product ions extracted at the end of the reaction-observation window can be modelled quantitatively. Examples of such TOF distributions recorded for windows of duration τ increasing from 1 to 6 μs are depicted in Fig. 2, where the experimental TOF traces near the H_3^+ and H_2D^+ flight times are drawn as dashed grey and black lines, respectively. These distributions, which have been normalised to the same total integrated product signal for ease of comparison, rapidly change with increasing τ values. For the shortest window (τ = 1 μs) the product-ion TOF distributions are narrow and symmetric. As τ increases, they broaden and gradually develop a characteristic double-peak structure caused by the expansion of the products.

The peak on the late TOF side of the distribution corresponds to the product ions generated just before the extraction pulse and which are still located close to the reaction volume by the time the extraction pulse is applied. Its position is therefore independent of τ. The wings of the distribution on both sides of this peak originate from product ions formed earlier and which have had the time to expand out of the reaction volume. The earlier peak becomes noticeable in the range of τ from 3 to 4 μs and from 5 to 6 μs in the distributions of H_3^+ and H_2D^+, respectively, when the product ions generated at the beginning of the reaction-observation window have filled the entire product-ion extraction zone. It originates from a TOF-focussing effect affecting ions located close to the repeller plate of the extraction stack. These ions are accelerated by the largest potential difference and arrive earliest at the detector. In contrast, the product ions that have moved towards the detector are less strongly accelerated so that their times of flight are longer and subject to a strong dispersion. They form the weak tail on the long-TOF side of the distributions.

To model the TOF distributions in particle-trajectory simulations, we assume, as in our previous study of the $H_2^+ + H_2$ reaction[30,35] and based on the earlier results of Pollard *et al.* at a collision energy of 1.5 eV,[34] that the product ions of both reaction channels are emitted isotropically and that the overall shape of their recoil-energy (E_{kin}) distribution, $d\sigma/dE_{kin}$, corresponds to that determined experimentally by Pollard *et al.*[34] (see their Fig. 12a for $v' = 0$). We then scale the entire distribution linearly by adjusting the average product kinetic energy E_{mean} to achieve the best agreement between experimental and simulated distributions. To have a quantitative measure of this agreement and to estimate the error bar in E_{mean}, we integrate, for different values of E_{mean}, the simulated TOF distribution in narrow regions around the two maxima (*i.e.*, between 3.30 and 3.33 μs for the earlier peak of the H_2D^+ distribution and between 3.41 and 3.44 μs for the later peak) and compare the ratios of the integrated values with the ratios determined from the experimental data. The results of the comparison are presented in Fig. 3a, where the experimental ratios extracted from the TOF distributions of H_2D^+ measured for reaction-observation windows of 4, 5, and 6 μs are depicted as red, green and blue horizontal lines, respectively. The corresponding ratios derived from the simulated TOF distributions for different values of E_{mean} are plotted as red circles, green squares and blue triangles, respectively. The comparison restricts the possible range of E_{mean} to the area shaded in grey in Fig. 3a. The average product recoil energy is thus 0.46(5) eV, *i.e.*, 27(3)% of the available energy. The corresponding distribution of recoil energy is depicted in Fig. 3b.

The simulated TOF profiles obtained for E_{mean} = 0.46 eV are drawn in Fig. 2b in orange and red for H_3^+ and H_2D^+, respectively, and are in excellent agreement with the measured ones, which illustrates the reliability of this analysis. Fig. 3c displays the corresponding velocity distributions of the H_3^+ and H_2D^+ products, which peak at 3.45 and 2.05 km s^{-1}, respectively. Consequently, the fastest H_3^+ products reach the repeller plate of the electrode stack earlier than the fastest H_2D^+ products and, consequently, the earlier peak of the TOF profile of H_3^+ becomes noticeable at shorter reaction-observation windows in Fig. 2b than that of H_2D^+.

B. Relative reaction cross sections and branching ratios of the H_3^+ and H_2D^+ reaction channels

The large velocities of the product ions imply that, with increasing duration of the reaction-observation window, a growing fraction of

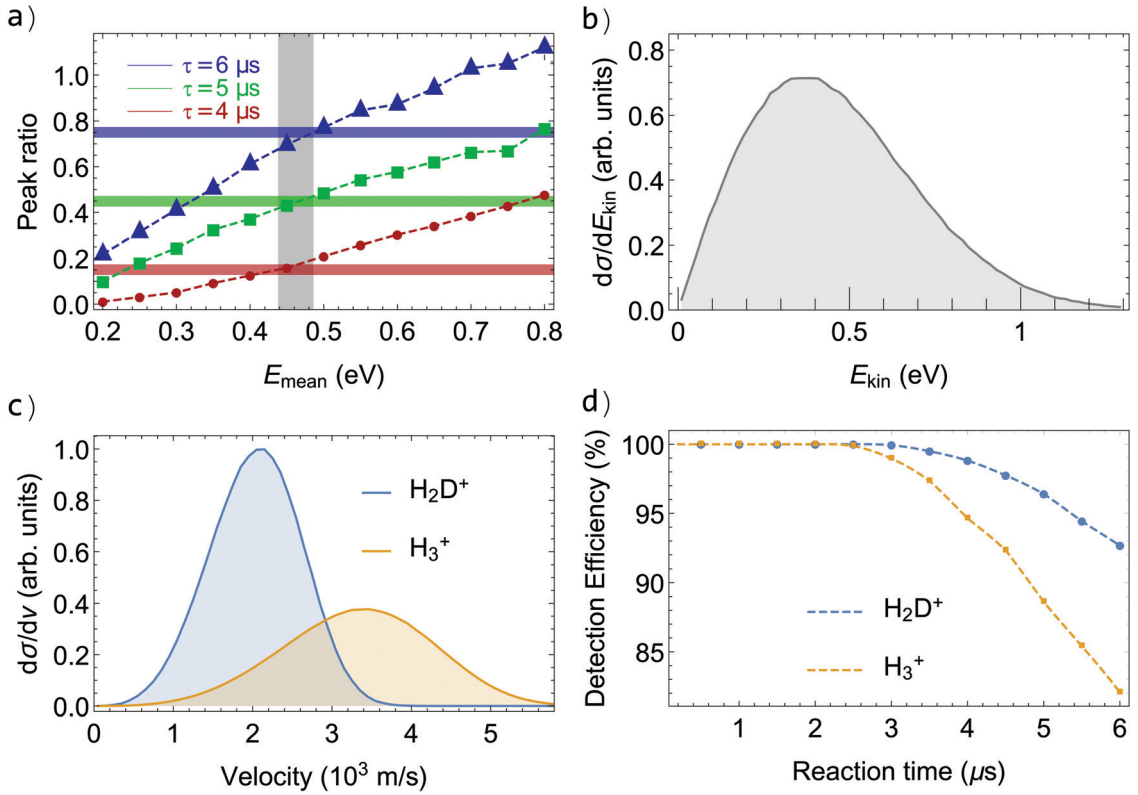

Fig. 3 Determination of the H_3^+ + D and H_2D^+ + H product branching ratios of the H_2^+ + HD reaction system. (a) Comparison of experimental and simulated ratios of the signal strength in the vicinity of the two maxima of the TOF distribution of H_2D^+ for reaction-observation windows with duration τ of 4 (red), 5 (green) and 6 μs (blue). Horizontal lines: experimental results; the experimental uncertainties are estimated to be comparable to the widths of the lines. Symbols connected by lines: simulation results. The grey shaded area corresponds to the possible range of the average of the kinetic energy of the products E_{mean}. (b) Total product-kinetic-energy distribution of the H_2^+ + HD reaction determined from experimental data. (c) Corresponding velocity distributions of H_3^+ (orange) and H_2D^+ (pale blue). (d) Normalised detection efficiency of H_3^+ (orange) and H_2D^+ (blue) as a function of the duration τ of the reaction-observation window, called reaction time.

these ions leaves the extraction region before the ion-extraction field is applied. Because of their different masses and recoil velocities, H_3^+ and H_2D^+ are not detected with the same efficiency, especially for the longer reaction-observation windows. These aspects do not affect measurements of the collision-energy dependence of the reaction cross sections because the range over which the collision energy is varied (about 3.5 meV) is negligible compared to $\Delta_r U^\circ(0\ \mathrm{K})$. However, they play an important role in the determination of the branching ratios of the H_3^+ + D and H_2D^+ + H reaction channels because H_2D^+ is detected more efficiently than the faster H_3^+ (see Fig. 3c and d).

Fig. 4 displays the relative total reaction cross section as a function of the collision energy between 0 and k_B·30 K in a double logarithmic plot. In the experiment, the velocity of the H_2-Rydberg beam was varied from 1270 to 2020 m s^{-1} whereas the velocity of the HD beam was kept fixed at 1390 m s^{-1}, as explained in Section II. The relative velocity was thus varied from −120 to 630 m s^{-1}, including ranges where the H_2-Rydberg beam was slower and faster than the HD-beam velocity. Consequently, the relative reaction cross sections were measured for both positive and negative relative velocities in the collision-energy range from 0 to k_B·1.5 K, as indicated by the full circles and squares in Fig. 4. The results of two sets of measurement carried out for reaction-observation windows of 5 and 6 μs duration are presented in Fig. 4 as blue and red data points, respectively. For each data point, the grey horizontal bar indicates the range of collision energies probed experimentally (see eqn (4)) and the vertical bar represents the statistical uncertainty (one standard deviation). In a double-logarithmic representation (Fig. 4), the two data sets are perfectly described by a linear function and a linear regression gives a slope of −0.505(14), which is consistent with the $E_{coll}^{-1/2}$ dependence of Langevin-capture reactions. In contrast to the behaviour observed in our investigation of the $H_2^+ + H_2$ reaction, no deviation from Langevin-capture behaviour is noticeable in Fig. 4 within the uncertainty limit of our measurements. We attribute this difference to the fact that the HD molecules are all in the $X\ ^1\Sigma_g^+(v = 0, J = 0)$ ground state, which rules long-range ion–quadrupole interactions out. In our studies of the $H_2^+ + H_2$ reaction, we used a natural H_2 sample, with 75% of the population in the $J = 1$ rotational level (ortho-H_2), which has a quadrupole moment causing the deviation from Langevin-capture behaviour.[25,30] Our ability to accurately model the observed TOF and kinetic-energy distributions of the product ions in particle-trajectories simulations makes it possible to extract the detection efficiencies of the H_3^+ and H_2D^+ product ions as a function of the duration of the reaction-observation window. These efficiencies

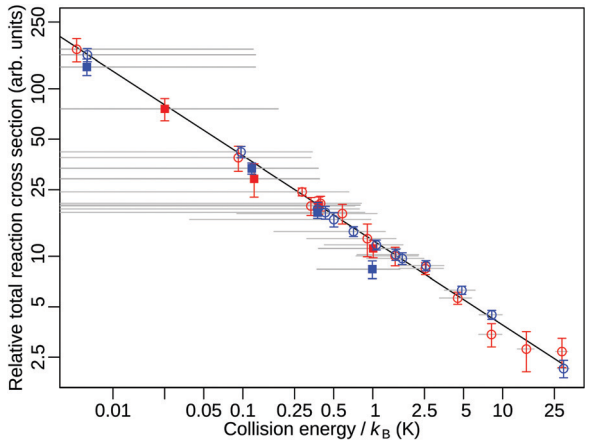

Fig. 4 Relative total reaction cross section for the H_2^+ + HD reaction in the range of collision energies between 0 and k_B·30 K. The horizontal grey bars represent the range of collision energies probed experimentally and the vertical error bars represent one standard deviation of the individual data points. The full line, with an exponent of −0.505(14) was obtained by linear regression. Circles and squares indicate that the velocity of the H_2-Rydberg beam was slower and faster than the HD beam, respectively. The blue and red data points were obtained for τ values of 5 and 6 μs, respectively.

are displayed as orange and blue dashed lines in Fig. 3d. They indicate that almost no product ions are lost when the reaction-observation window does not exceed 3 μs but that almost 20% and 8% of the H_3^+ and H_2D^+ product ions are lost, respectively, when the reactions products are extracted after 6 μs. It is therefore necessary to correct the ion signals for these losses when determining the branching ratios of the H_3^+ + D and H_2D^+ + H product channels from measurements carried out at τ values of more than about 3 μs.

The top panel in Fig. 5 presents the measured signal ratios $I(H_3^+)/[I(H_3^+) + I(H_2D^+)]$ as a function of τ as black dots. The turquoise diamonds indicate the corresponding ratios expected from the simulations after scaling to a value of 0.225 at τ = 0. The good agreement between the measured and simulated ratios enables us to derive the corrected branching ratios displayed in the bottom panel of Fig. 5. At short values of τ, the product-ion signals are weak and thus subject to large statistical uncertainties. The signals increase with increasing value of τ but beyond about 6 μs, the systematic deviation associated with the different detection efficiency of H_3^+ and H_2D^+ becomes significant. We therefore determine the branching ratio and its uncertainty from the measurements carried out at $\tau \leq$ 6 μs, as indicated by the full and dashed red lines in Fig. 5b, which correspond to a branching ratio of 0.225(10) for the H_3^+ + D reaction channel. Taking the systematic uncertainty, which is comparable to the statistical one, into account leads to a branching ratio of 0.225(20).

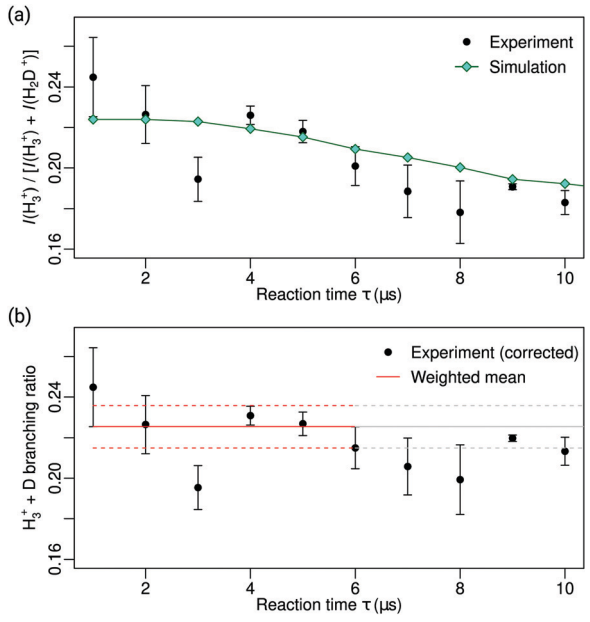

Fig. 5 (a) Measured $I(H_3^+)/[I(H_3^+) + I(H_2D^+)]$ product ratio as a function of the duration τ of the reaction-observation window (reaction time). The green trace with turquoise diamonds represents the ratios expected from the simulations after scaling to a value of 0.225 at τ = 0. (b) H_3^+ + D product branching ratio corrected for the detection efficiency. The vertical error bars indicate one standard deviation of the individual data points, and the full and dashed red lines represent the weighted mean and its standard deviation, respectively.

IV Conclusions

In this article we have presented improvements in the design and operation of a merged-beams apparatus developed recently to study ion–molecule reactions at low collision energies.[35] These improvements include a better collimation of the pulsed supersonic gas beams, more sensitive and reliable diagnostic tools for the characterisation and optimisation of the temporal, spatial and velocity distributions of the gas pulses, and the optimisation of the plunger-driving mechanism of the pulsed valves to avoid the emission of secondary pulses caused by the plunger rebounce. In combination with the development of a more stable optomechanical layout and of optimised electric-pulse sequences to extract the product ions, these measures have led to an improvement of the collision-energy resolution of our measurements by a factor of four, *i.e.*, reaching 75 mK at the lowest collision energies. They have also enabled us to measure the kinetic-energy distributions of the product ions, from which information on the internal-state distribution of the product ions can be inferred.

We have used these improvements in a study of the two reaction channels of the reaction H_2^+ + HD, forming H_3^+ + D and H_2D^+ + H, at collision energies between 0 and k_B·30 K. A special feature of the experiment is the full state selection of the reactants, both H_2^+ and HD being in their ground rovibronic state. The main scientific results obtained on this reaction system are (i) the determination of the energy dependence of the total reaction cross section, (ii) the determination of the product-kinetic-energy distribution, and (iii) the measurement of branching ratios for the two reaction channels. Concerning (i), our new data exhibit Langevin-capture behaviour down to

the lowest collision energies accessible, *i.e.*, ≈50 mK. This observation indicates that the very small dipole moment of HD plays no role, as expected, and is attributed to the absence of the ion–quadrupole long-range interaction because HD is in its $J = 0$ ground state. This behaviour differs from what was observed in the reaction of $H_2^+ + H_2$, where the quadrupole in the $J = 1$ ground state of ortho H_2 led to an enhancement of the reaction cross section compared to the Langevin-capture value below collision energies of $k_B \cdot 1$ K.[30]

The mean kinetic energy of the products was found to be 0.46(5) eV. With the dissociation energies of H_2,[52] HD,[53] H_2^+[31] and H_3^+[32] and the zero-point vibrational energies of H_3^+,[32] H_2D^+,[54] H_2 and HD,[55] the exothermicity ($\Delta_r U^\circ(0\ K)$) of the reactions (1) and (2) can be estimated to be −1.662 and −1.718 eV, respectively. Consequently, 27(3)% of the available energy is transferred as product kinetic energy, slightly less than the value of 32% found by Pollard *et al.* in their study of the $H_2^+ + H_2 \rightarrow H_3^+ + H$ at a collision energy of 1.5 eV,[34] but in excellent agreement with the value of 28% predicted by Eaker and Schatz[33] for this reaction. Our results therefore indicate that the H_3^+ and H_2^+D ions are produced with an average of about 1.25 eV of rovibrational energy. No significant effects of a possible forward–backward asymmetry on the product distribution could be detected at the low collision energies of our study.

The branching ratio of the channel forming $H_3^+ + D$ was found to be 0.225(20). This ratio is close to, but slightly below, the value of 0.25 one would obtain by randomly choosing the atomic fragment from the H_3D^+ collision complex. Previous studies of this reaction have shown that it follows a direct stripping mechanism[28,34,47–50] so that the agreement of the branching ratio observed experimentally with the prediction of this combinatorial argument is likely to be accidental. The observation might be related to the slight preference for a D-atom hop over an H-atom hop from HD to H_2^+ at very low collision energies predicted by Sanz-Sanz *et al.*[28] (see their Fig. 12). A characteristic of our new experimental results is that they are obtained in the collision-energy range where the charge-transfer reaction (eqn (3)) is energetically forbidden. The charge transfer process is allowed at the lowest collision energies for the reaction $HD^+ + H_2$ and we are currently adapting our measurement procedure to study this reaction.

Conflicts of interest

There are no conflicts of interest to declare.

Acknowledgements

We thank Dr Valentina Zhelyazkova, Dr Matija Žeško and Fernanda B. V. Martins for useful discussions on all aspects of the experiment, Prof. Manuel Lara and Prof. Octavio Roncero, Madrid, for useful discussions and Prof. Octavio Roncero for sharing with us the results of preliminary calculations of the product branching ratios of the $H_2^+ + D_2$ reaction. This work is supported by the Swiss National Science Foundation (Grant No. 200020-172620) and the European Research Council (ERC) under the European Unions Horizon 2020 research and innovation programme (Advanced Grant No. 743121).

References

1 A. B. Henson, S. Gersten, Y. Shagam, J. Narevicius and E. Narevicius, *Science*, 2012, **338**, 234.
2 J. Jankunas, B. Bertsche, K. Jachymski, M. Hapka and A. Osterwalder, *J. Chem. Phys.*, 2014, **140**, 244302.
3 Y. Shagam, A. Klein, W. Skomorowski, R. Yun, V. Averbukh, C. P. Koch and E. Narevicius, *Nat. Chem.*, 2015, **7**, 921.
4 J. Jankunas and A. Osterwalder, *Annu. Rev. Phys. Chem.*, 2015, **66**, 241.
5 W. E. Perreault, N. Mukherjee and R. N. Zare, *Science*, 2017, **358**, 356.
6 J. Zou, S. D. S. Gordon and A. Osterwalder, *Phys. Rev. Lett.*, 2019, **123**, 133401.
7 N. Bibelnik, S. Gersten, A. B. Henson, E. Lavert-Ofir, Y. Shagam, W. Skomorowski, C. P. Koch and E. Narevicius, *Mol. Phys.*, 2019, **117**, 2128.
8 A. D. Dörfler, P. Eberle, D. Koner, M. Tomza, M. Meuwly and S. Willitsch, *Nat. Commun.*, 2019, **10**, 5429.
9 J. B. Marquette, B. R. Rowe, G. Dupeyrat, G. Poissant and C. Rebrion, *Chem. Phys. Lett.*, 1985, **122**, 431.
10 D. Gerlich, in *Low Temperatures and Cold Molecules*, ed. I. M. W. Smith, Imperial College Press, London, 2008, ch. 3, pp. 121–174.
11 T. D. Tran, S. Rednyk, A. Kovalenko, Š. Roučka, P. Dohnal, R. Plašil, D. Gerlich and J. Glosík, *Astrophys. J.*, 2018, **854**, 25.
12 C. R. Markus, O. Asvany, T. Salomon, P. C. Schmid, S. Brünken, F. Lipparini, J. Gauss and S. Schlemmer, *Phys. Rev. Lett.*, 2020, **124**, 233401.
13 *Kinetics of Ion-Molecule Reactions*, ed. P. Ausloos, Nato Advanced Study Institute Series – Series B: Physics, Plenum Press, New York, 1978, vol. 40.
14 *Gas Phase Ion Chemistry: Vol. 1 and 2*, ed. M. T. Bowers, Academic Press, New York, 1979.
15 *State-selected and state-to-state ion-molecule reaction dynamics: Part 1. Experiment and Part 2. Theory*, ed. C.-Y. Ng and M. Baer, Advances in Chemical Physics, John Wiley & Sons, Inc., New York, 1992, vol. 82.
16 D. C. Clary, *Mol. Phys.*, 1985, **54**, 605.
17 J. Troe, *J. Chem. Phys.*, 1987, **87**, 2773.
18 D. C. Clary, D. Smith and N. G. Adams, *Chem. Phys. Lett.*, 1985, **119**, 320.
19 D. C. Clary, *Annu. Rev. Phys. Chem.*, 1990, **41**, 61.
20 T. Stoecklin, D. C. Clary and A. Palma, *J. Chem. Soc., Faraday Trans.*, 1992, **88**, 901.
21 J. Troe, *J. Chem. Phys.*, 1996, **105**, 6249.
22 M. Auzinsh, E. I. Dashevskaya, I. Litvin, E. E. Nikitin and J. Troe, *J. Chem. Phys.*, 2013, **139**, 084311.
23 M. Auzinsh, E. I. Dashevskaya, I. Litvin, E. E. Nikitin and J. Troe, *J. Chem. Phys.*, 2013, **139**, 144315.

24 E. I. Dashevskaya, I. Litvin, E. E. Nikitin and J. Troe, *J. Chem. Phys.*, 2005, **122**, 184311.
25 E. I. Dashevskaya, I. Litvin, E. E. Nikitin and J. Troe, *J. Chem. Phys.*, 2016, **145**, 244315.
26 T. Oka, *Chem. Rev.*, 2013, **113**, 8738.
27 T. Glenewinkel-Meyer and D. Gerlich, *Isr. J. Chem.*, 1997, **37**, 343.
28 C. Sanz-Sanz, A. Aguado, O. Roncero and F. Naumkin, *J. Chem. Phys.*, 2015, **143**, 234303.
29 I. Savić, S. Schlemmer and D. Gerlich, *ChemPhysChem*, 2020, **21**, 1429.
30 P. Allmendinger, J. Deiglmayr, K. Höveler, O. Schullian and F. Merkt, *J. Chem. Phys.*, 2016, **145**, 244316.
31 V. I. Korobov, L. Hilico and J.-P. Karr, *Phys. Rev. Lett.*, 2017, **118**, 233001.
32 I. I. Mizus, O. L. Polyansky, L. K. McKemmish, J. Tennyson, A. Alijah and N. F. Zobov, *Mol. Phys.*, 2019, **117**, 1663.
33 C. W. Eaker and G. C. Schatz, *J. Phys. Chem.*, 1985, **89**, 2612.
34 J. E. Pollard, L. K. Johnson, D. A. Lichtin and R. B. Cohen, *J. Chem. Phys.*, 1991, **95**, 4877.
35 P. Allmendinger, J. Deiglmayr, O. Schullian, K. Höveler, J. A. Agner, H. Schmutz and F. Merkt, *ChemPhysChem*, 2016, **17**, 3596.
36 S. T. Pratt, J. L. Dehmer, P. M. Dehmer and W. A. Chupka, *J. Chem. Phys.*, 1994, **101**, 882.
37 M. Matsuzawa, *Phys. Rev. A: At., Mol., Opt. Phys.*, 2010, **82**, 054701.
38 E. Wrede, L. Schnieder, K. Seekamp-Schnieder, B. Niederjohann and K. H. Welge, *Phys. Chem. Chem. Phys.*, 2005, **7**, 1577.
39 D. Dai, C. C. Wang, G. Wu, S. A. Harich, H. Song, M. Hayes, R. T. Skodje, X. Wang, D. Gerlich and X. Yang, *Phys. Rev. Lett.*, 2005, **95**, 013201.
40 S. R. Procter, Y. Yamakita, F. Merkt and T. P. Softley, *Chem. Phys. Lett.*, 2003, **374**, 667.
41 E. Vliegen, H. J. Wörner, T. P. Softley and F. Merkt, *Phys. Rev. Lett.*, 2004, **92**, 033005.
42 S. D. Hogan, P. Allmendinger, H. Sassmannshausen, H. Schmutz and F. Merkt, *Phys. Rev. Lett.*, 2012, **108**, 063008.
43 V. Zhelyazkova, M. Žeško, H. Schmutz, J. A. Agner and F. Merkt, *Mol. Phys.*, 2019, **117**, 2980.
44 P. Allmendinger, J. Deiglmayr, J. A. Agner, H. Schmutz and F. Merkt, *Phys. Rev. A: At., Mol., Opt. Phys.*, 2014, **90**, 043403.
45 M. Žeško, *Spectroscopic and atom-optics experiments on Rydberg He in electric and magnetic fields: towards low-temperature investigations of ion–molecule chemistry involving He^+*, PhD thesis, Eidgenössische Technische Hochschule Zürich, ETH Zürich, CH-8093 Zürich, Switzerland, 2019, Diss. ETH Nr. 26290.
46 V. Zhelyazkova, F. B. V. Martins, H. Schmutz, J. A. Agner and F. Merkt, *Phys. Rev. Lett.*, 2020, **125**, 263401.
47 A. B. Lees and P. K. Rol, *J. Chem. Phys.*, 1974, **61**, 4444.
48 J. R. Krenos, K. K. Lehmann, J. C. Tully, P. M. Hierl and G. P. Smith, *Chem. Phys.*, 1976, **16**, 109.
49 C. H. Douglass, D. J. McClure and W. R. Gentry, *J. Chem. Phys.*, 1977, **67**, 4931.
50 P. M. Hierl and Z. Herman, *Chem. Phys.*, 1980, **50**, 249.
51 Ch. Seiler, S. D. Hogan and F. Merkt, *Phys. Chem. Chem. Phys.*, 2011, **13**, 19000.
52 M. Beyer, N. Hölsch, J. Hussels, C.-F. Cheng, E. J. Salumbides, K. S. E. Eikema, W. Ubachs, Ch. Jungen and F. Merkt, *Phys. Rev. Lett.*, 2019, **123**, 163002.
53 D. Sprecher, J. Liu, Ch. Jungen, W. Ubachs and F. Merkt, *J. Chem. Phys.*, 2010, **133**, 111102.
54 J. Ramanlal, O. L. Polyansky and J. Tennyson, *Astron. Astrophys.*, 2003, **406**, 383.
55 K. P. Huber and G. Herzberg, *Molecular Spectra and Molecular Structure, Volume IV, Constants of Diatomic Molecules*, Van Nostrand Reinhold Company, New York, 1979.